Mutual optical intensity propagation through non-ideal mirrors

Xiangyu Meng,[a,b] Xianbo Shi,[c*] Yong Wang,[a*] Ruben Reininger,[c] Lahsen Assoufid[c] and Renzhong Tai[a*]

[a]Shanghai Institute of Applied Physics, Chinese Academy of Sciences, Zhangheng Road 239, Pudong District, Shanghai 201800, People's Republic of China, [b]University of Chinese Academy of Sciences, Yuquan Road 19, Shijingshan District, Beijing 100049, People's Republic of China, and [c]Advanced Photon Source, Argonne National Laboratory, 9700 South Cass Avenue, Argonne, IL 60439, USA. *Correspondence e-mail: xshi@aps.anl.gov, wangyong@sinap.ac.cn, tairenzhong@sinap.ac.cn

The mutual optical intensity (MOI) model is extended to include the propagation of partially coherent radiation through non-ideal mirrors. The propagation of the MOI from the incident to the exit plane of the mirror is realised by local ray tracing. The effects of figure errors can be expressed as phase shifts obtained by either the phase projection approach or the direct path length method. Using the MOI model, the effects of figure errors are studied for diffraction-limited cases using elliptical cylinder mirrors. Figure errors with low spatial frequencies can vary the intensity distribution, redistribute the local coherence function and distort the wavefront, but have no effect on the global degree of coherence. The MOI model is benchmarked against *HYBRID* and the multi-electron *Synchrotron Radiation Workshop* (*SRW*) code. The results show that the MOI model gives accurate results under different coherence conditions of the beam. Other than intensity profiles, the MOI model can also provide the wavefront and the local coherence function at any location along the beamline. The capability of tuning the trade-off between accuracy and efficiency makes the MOI model an ideal tool for beamline design and optimization.

1. Introduction

Modern X-ray synchrotron radiation facilities and free-electron laser sources provide beams with high brilliance and a high degree of coherence. Knowledge of the degree of coherence and the quality of the wavefront at the sample is essential for many experimental techniques, such as X-ray photon correlation spectroscopy (Stephenson *et al.*, 2009), X-ray interference lithography (Zhang *et al.*, 2014) and coherent X-ray diffraction imaging (Nugent, 2010). There is a high demand for simulation tools to analyze the beam coherence properties along synchrotron radiation beamlines.

Several simulation packages have been developed for the propagation of partially coherent beams through beamline optics. The *SRW* code (Chubar, 2014; Samoylova *et al.*, 2011) calculates the spontaneous emission of electrons through magnetic fields, and simulates the wavefront propagation through optical elements and free space based on the Fourier optics approach. The multi-electron *SRW* is the most advanced code dealing with partially coherent radiation. The main disadvantage of *SRW* is that only limited information is extracted and stored at the observation plane, and this information cannot be carried over directly to another plane. *HYBRID* (Shi *et al.*, 2014a,b) combines ray tracing and wavefront propagation, and it provides an efficient approach to calculate beam intensity profiles along the beamline. *HYBRID* uses *SHADOW* (Sanchez del Rio *et al.*, 2011) as
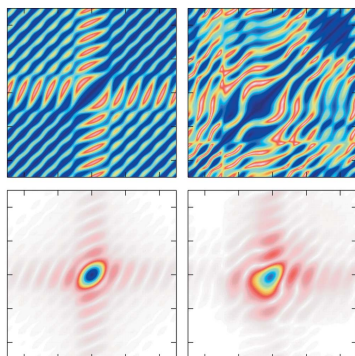
its backbone to simulate the geometric effects of optical elements, whereas their diffraction contributions are calculated using wavefront propagation. The results from the diffraction and geometric effects are integrated together by numerical convolution and ray re-sampling. The mutual optical intensity (MOI) model was recently developed based on statistical optics to simulate partially coherent radiation propagation through X-ray optics (Meng *et al.*, 2015). The model is based on the MOI function that describes both the wavefront and the coherence property of the beam. The wavefront is separated into many small elements to perform the numerical calculation of MOI propagation through free space. Combined with the local ray tracing, MOI propagation through ideal mirrors and gratings was realised (Meng *et al.*, 2015). The main aim of the MOI method is to provide the full coherence property of the beam, which can also be realised by the propagation of the cross-spectral density function (Singer & Vartanyants, 2014; Vartanyants & Singer, 2016).

Accurate simulation models based on wave optics are necessary to study the influence of figure errors to ensure that the photon beam is not impaired. In this paper, we extend the MOI model to calculate the propagation of a partially coherent beam through mirrors with figure errors. Using both the phase projection and direct path length approaches, figure errors of different spatial frequencies are studied and compared, and the results allow the assessment of the capability and limitation of the method. The MOI model is benchmarked against *SRW* and *HYBRID* on the simulation of partially coherent beam propagation. Unlike *HYBRID*, the MOI model provides not only the intensity profile but also wavefront and coherence information of the beam. Since the full coherence function is stored, the result at one plane can be carried over and used to propagate to another plane, which is an advantage of the MOI model over *SRW*. Furthermore, the accuracy of the calculation can be improved by increasing the number of wavefront elements at the cost of simulation time. The capability of switching between fast rough estimation and slow accurate calculation makes the MOI model a powerful tool for beamline design.

2. Method description

2.1. MOI propagation through free space

The MOI propagation through free space was reported in previous work (Meng *et al.*, 2015) and is summarized here. The four-dimensional MOI, $J(P_1, P_2)$, describes the electric field distribution and the correlation between any two points P_1 and P_2. The propagation of MOI from the source plane $J(P_1, P_2)$ to the image plane $J(Q_1, Q_2)$ through free space is represented by the equation (Goodman, 2015; Mandel & Wolf, 1995)

$$J(Q_1, Q_2) = \iint \iint J(P_1, P_2) \exp\left[-i(2\pi/\lambda)(r_2 - r_1)\right]$$
$$\times \frac{\chi(\theta_1)}{\lambda r_1} \frac{\chi(\theta_2)}{\lambda r_2} \, dS_1 \, dS_2, \qquad (1)$$

where λ is the wavelength, r_1 and r_2 are the P_1-to-Q_1 and P_2-to-Q_2 distances, respectively; $\chi(\theta_1)$ and $\chi(\theta_2)$ are the inclination factors for the inclination angles θ_1 and θ_2, respectively; and S_1 and S_2 are the surfaces of the source. The MOI propagation through free space based on equation (1) is carried out by a numerical procedure. Firstly, the source plane is separated equally into many elements, assuming that the beam has constant complex amplitude and full coherence in each element. This assumption is valid when the size of the element is much smaller than the beam size and the transverse coherence length. Secondly, the propagation of each element of the MOI is calculated with the Fraunhofer or Fresnel approximation (Born & Wolf, 1999). Finally, the MOI at the image plane is obtained by summing the contributions of all elements, or

$$J(Q_1, Q_2) = \sum_{mn} \left[A^*_{mnQ_2} \sum_{jk} J(P_{jk}, P_{mn}) A_{jkQ_1} \right], \qquad (2)$$

where j, k, m and n are the element indexes at the source plane, and with

$$A_{jkQ_1} = \iint \exp\left[i(2\pi/\lambda) r_{P_{jk}Q_1}\right] \frac{\chi(\theta_1)}{\lambda r_{P_{jk}Q_1}} \, dS_{jk}. \qquad (3)$$

2.2. MOI propagation through ideal mirrors

The MOI propagation through reflecting mirrors is carried out using local ray tracing from the incident plane to the exit plane. The incident and exit planes are at zero distance from the center of the mirror as shown in Fig. 1, and perpendicular to the incident and exit beam axes, respectively. Rays are first generated on a regular position mesh at the incident plane. The rays travel along the direction defined by the local phase gradient of the X-ray wave, intersect with and reflect from the mirror surface, and hit the exit plane. The ray-tracing step generates a coordinate transformation between the exit and incident planes and the path length, which are used in the MOI integration below.

In this paper, we focus on the propagation in one transverse direction for demonstration purposes. The spatial coordinates of the incident and exit planes are defined in $P(u, v)$ and $Q(x, y)$, respectively. The longitudinal axes v and y are the directions of the beam propagation, while u and x are the transverse axes (*cf.* Fig. 1). The propagation of MOI from the
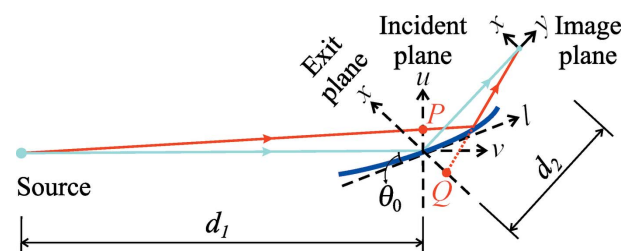

Figure 1
Schematic layout of the MOI propagation through a mirror.

incident plane $J_i(P_1, P_2)$ to the exit plane $J_e(Q_1, Q_2)$ is described as follows (Goodman, 2015; Meng *et al.*, 2015),

$$J_e(Q_1, Q_2) = J_i[\tilde{P}(Q_1), \tilde{P}(Q_2)] \, t[\tilde{P}(Q_1)] \, t^*[\tilde{P}(Q_2)]$$
$$\times \exp\Big(i(2\pi/\lambda)\{\Gamma[Q_1, \tilde{P}(Q_1)] - \Gamma[Q_2, \tilde{P}(Q_2)]\}\Big)$$
(4)

where $\tilde{P}(Q)$ is the coordinate transformation function between the incident and exit planes, $\Gamma(Q, P)$ is the path length between the two planes obtained from the local ray tracing using the ideal mirror surface functions, and $t(P)$ is the complex amplitude transmission function.

Unlike the wavefront propagation code based on fast Fourier transform (Canestrari *et al.*, 2014), the electric field components do not need to be interpolated onto regular grids. Instead, the interpolation is done in the integration step through amplitude scaling. Since the transformation between the incident coordinate (u) and the exit coordinate (x) is non-linear, the amplitude of the wavefront in each element is scaled based on the local coordinate step sizes. The complex amplitude transmission function through the mirror is expressed as

$$t(x) = (du/dx)^{1/2},$$
(5)

where the reflectivity of the mirror is taken as 1 for simplicity (no diffuse reflection considered here). The distribution of the path length $\Gamma(Q, P)$ projected at the exit plane is close to a parabola profile at small divergence angles. However, the parabola profile should be amended at larger divergence angles. It is assumed that each element has its own parabola profile and is different from the others.

The MOI propagation through a mirror can be performed in three steps: (i) free-space propagation from the source plane to the incident plane using equation (2); (ii) propagation from the incident plane to the exit plane using equation (4); and (iii) propagation from the exit plane to the image plane using equation (2).

2.3. MOI propagation through non-ideal mirrors

Real mirrors have figure errors, which can be considered as phase shifts within the paraxial and smooth mirror approximation (Shi *et al.*, 2014b). Two methods are introduced into the MOI model dealing with figure errors: the phase projection method (MOI option 1) and the direct path length method (MOI option 2).

MOI option 1 comes from *HYBRID* (Shi *et al.*, 2014a), in which the phase shifts are presented by adding an exponential term to the amplitude transmission function $t(x)$ analytically. The height error profile $\Delta h(l)$ in the mirror coordinate l is projected onto the exit plane coordinates x. The phase shift $\Delta\Phi_h(x)$ due to the figure error is thus

$$\Delta\Phi_h(x) = -(4\pi/\lambda)\Delta h(x)\sin\theta_0(x),$$
(6)

where $\theta_0(x)$ is the grazing angle of the mirror transformed in the exit plane coordinate. The amplitude transmission function becomes

$$t(x) = (du/dx)^{1/2}\exp[-i(4\pi/\lambda)\Delta h(x)\sin\theta_0(x)].$$
(7)

Combining equations (4) and (7), the MOI propagation through real mirrors can be carried out.

MOI option 2 deals with figure errors through the direct path length calculation. Local ray tracing is conducted from the incident plane through the mirror surface with figure errors to the exit plane. $t(x)$ is still the same as in equation (5) to account for the size and amplitude change of each element. The figure error effects are included directly in the path length terms $\Gamma[Q_1, \tilde{P}(Q_1)]$ and $\Gamma[Q_2, \tilde{P}(Q_2)]$ in equation (4). This direct path length method is valid when there is no crossing of local rays, which means the indexes of all elements remain the same.

2.4. Global degree of coherence

MOI contains the correlation information between any two points in the wavefront, from which the statistical coherence of the entire beam can be quantitatively obtained. The global degree of coherence (Vartanyants & Singer, 2010), ranging from 0 to 1, is a spatial average of the transverse degree of coherence, given as

$$G = \frac{\int\limits_{-\infty}^{\infty} |J(x_1, z_1, x_2, z_2)|^2 \, dx_1 \, dz_1 \, dx_2 \, dz_2}{\left[\int\limits_{-\infty}^{\infty} I(x, z) \, dx \, dz\right]^2},$$
(8)

where $I(x, z)$ is the intensity distribution of the beam in the transverse coordinates (x, z).

3. MOI propagation through focusing mirrors

When the X-ray source has a narrow angular divergence, the MOI can be simplified by using the Gaussian Schell Model (GSM) (Vartanyants & Singer, 2010; Pelliccia *et al.*, 2011). The spatial distributions of the intensity and the degree of coherence are both Gaussian functions. The MOI in one transverse direction x is given by

$$J(x_1, x_2) = I_0\left[\exp\left(-\frac{x_1^2 + x_2^2}{2\sigma_x^2}\right)\right]^{1/2}\exp\left[-\frac{(x_1 - x_2)^2}{2\xi_x^2}\right],$$
(9)

where I_0 is a constant representing the maximum intensity, and σ_x and ξ_x define the size and the transverse coherence length of the source, respectively. The parameters of a GSM source satisfy the following equation:

$$\frac{(2\pi\sigma_x')^2}{\lambda^2} = \frac{1}{4\sigma_x^2} + \frac{1}{\xi_x^2},$$
(10)

where σ_x' denotes the angular divergence of the beam (Vartanyants & Singer, 2010; Hua *et al.*, 2013).

The developed MOI model is used to analyze a diffraction-limited focusing case (Shi *et al.*, 2014a), in which the optical layout and coordinate definition are shown in Fig. 1. The 10 keV source is assumed Gaussian with an RMS size of 2 µm and an RMS divergence of 30 µrad. The source-to-mirror distance is $d_1 = 30$ m. The focusing mirror has a length of $L =$
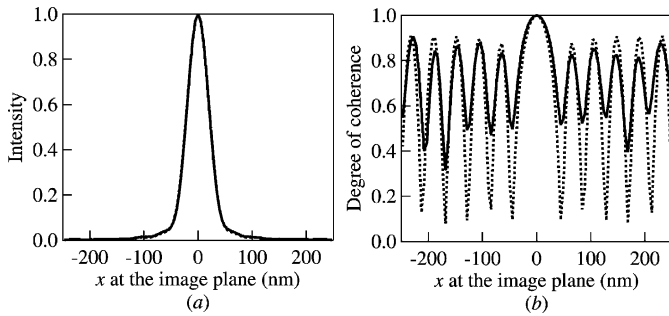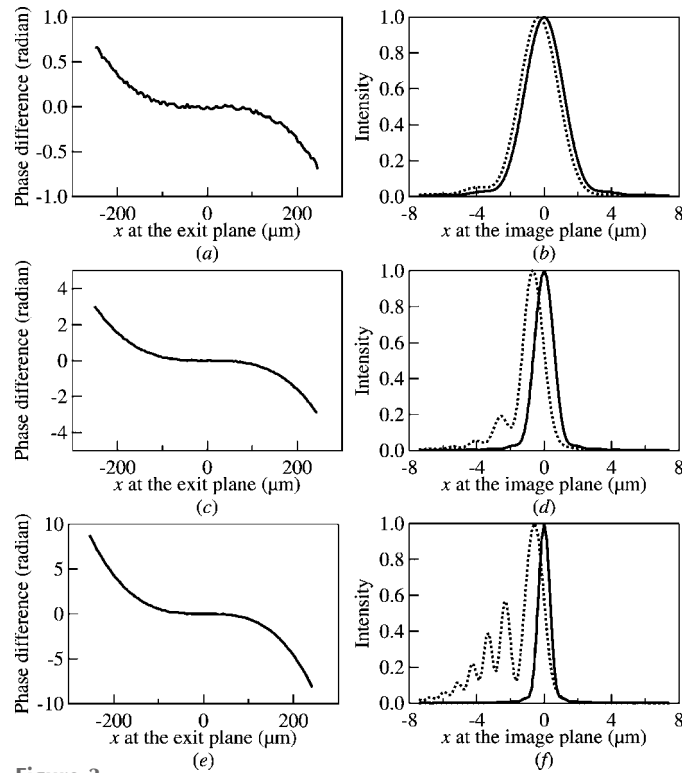
Figure 2
(a) Normalized intensity profiles and (b) distributions of the local degree of coherence at the image plane calculated by the MOI model. The solid lines and dotted lines denote the results of the elliptical cylinder mirror and the ideal thin lens, respectively. The numbers of elements used in the MOI calculation are 300, 300, 300 and 100 at the source, incident, exit and image planes, respectively.

200 mm and a grazing-incident angle of 2.5 mrad. The coherence length ξ_x at the source plane is 0.667 µm according to equation (10). The wavefront at all planes is divided into equal elements whose sizes are small enough to fulfil the Fresnel condition (Born & Wolf, 1999). The MOI at the incident plane is obtained by the free-space propagation based on equation (2).

We first compare the MOI propagation through an ideal thin lens and an elliptical cylinder mirror without figure errors. The mirror-to-image distance is chosen to be $d_2 = 0.2$ m. The path length through the ideal lens is described by the equation $\exp(-x^2/2f_x)$ with focal length $f_x = d_1 d_2/(d_1 + d_2)$. For the elliptical cylinder, the path length in equation (4) is calculated from local ray tracing by using the elliptical surface function (Marr, 2013). As shown in Fig. 2(a), the calculated intensity profiles of the two cases are almost identical. The MOI function also contains the full information of the local coherence, which is the phase correlation between any two points in the plane. Fig. 2(b) shows the local degree of coherence between any point and the central point. The two cases have the same oscillation pattern, which originates from the diffraction of the finite lens/mirror aperture (Meng et al., 2015). The difference in the degree of coherence amplitude is an indication that the elliptical cylinder mirror is not an exact ideal lens for non-point-to-point focusing cases.

We now compare the results obtained using the MOI model for an elliptical cylinder and a spherical cylinder for three mirror-to-image distances, d_2 = 3 m, 5 m and 10 m. The spherical cylinder suffers from coma aberration especially for strong demagnification cases. The phase difference between the elliptical and spherical cylinder mirrors is given by $\Delta\varphi = (2\pi/\lambda)(\Gamma_{ell} - \Gamma_{sph})$, where Γ_{ell} and Γ_{sph} are the path lengths between the incident and exit planes in the elliptical cylinder and the spherical cylinder cases, respectively. $\Delta\varphi$ is plotted in Figs. 3(a), 3(c) and 3(e) for the three d_2 distances. The phase difference becomes significant as d_2 decreases, and this gives rise to larger focal spot sizes at the image plane as shown in Figs. 3(b), 3(d) and 3(f). The oscillatory behavior on the beam profiles of spherical cylinder mirrors in Figs. 3(d) and 3(f) is a result of the interference effect, which was demonstrated by

Figure 3
(a, c, e) Phase difference at the exit plane between the elliptical and the spherical cylinder mirrors, and (b, d, f) intensity profiles at the image plane calculated with different mirror-to-image distances of (a, b) 10 m, (c, d) 5 m and (e, f) 3 m. Solid and dotted lines are the intensity profiles calculated using the elliptical cylinder and the spherical cylinder, respectively. The number of elements used in the MOI model is 100 at all calculation planes.

others (Bahrdt, 2007). In these studies, the mirrors also cut the beam, which gives rise to the small shoulder diffraction peaks in all intensity profiles.

In a general way, the mirror figure error profiles can be generated with (Shi et al., 2016)

$$\Delta h(l) = \sum_n b_0\, n^{s_0/2} \cos\left(\frac{2\pi n}{L}\, l + \psi_n\right), \tag{11}$$

where b_0 is a scaling factor in length units, n is the spatial frequency, s_0 is a parameter related to the power spectrum density function of the figure error and is chosen to be -3.0 in this paper to match the metrology data of an existing mirror (Siewert et al., 2012), and ψ_n is a random phase.

The propagation through the same mirror ($d_2 = 0.2$ m) is analyzed with figure errors of different spatial frequencies. Three figure error profiles with different frequency ranges n = 1–10, 11–100 and 101–1000 are used for the elliptical cylinder mirror. Three methods are used to calculate the phase shifts due to figure errors and the intensity profiles at the image plane: *HYBRID*, the phase projection method (MOI option 1) and the direct path length method (MOI option 2) (defined in §2.3). The results are shown in Fig. 4. In cases of low (n = 1–10) and medium (n = 11–100) frequencies, there is almost no difference in the phase shifts and intensity profiles from the two MOI methods. For the high-frequency (n = 101–
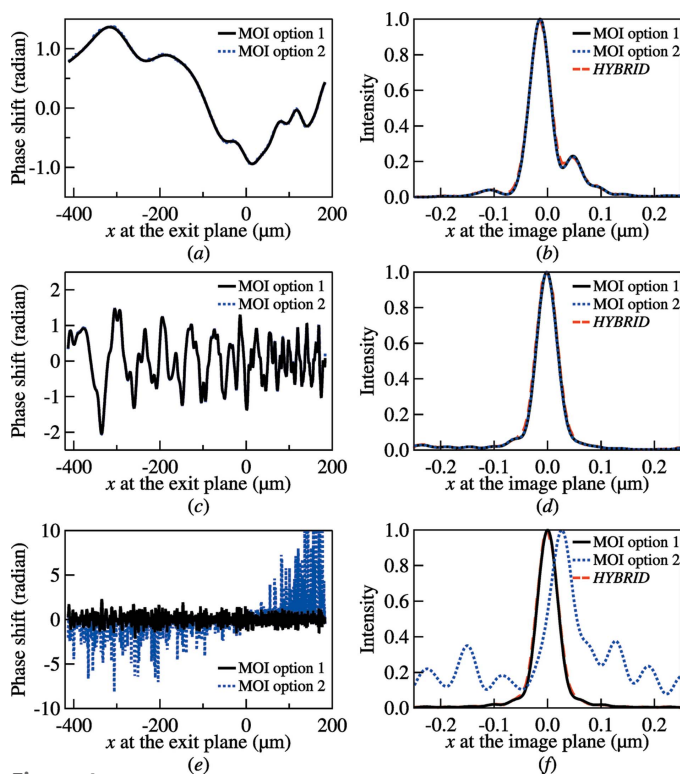
Figure 4

(a, c, e) Phase shifts due to figure errors, and (b, d, f) intensity profiles at the image plane calculated with different figure error profiles generated using equation (11) with (a, b) $b_0 = 1.1 \times 10^{-3}$ nm, $n = 1–10$, (c, d) $b_0 = 1.7 \times 10^{-2}$ nm, $n = 11–100$ and (e, f) $b_0 = 0.16$ nm, $n = 101–1000$. The RMS figure height error is 2.3 nm for all mirrors. Solid, dotted and dashed lines denote the results from the phase projection method (MOI option 1), the direct path length method (MOI option 2) and *HYBRID*, respectively. 300 elements are used in the MOI calculation for the low-frequency (a, b) case at the incident and exit planes of the mirror, while 1000 elements are used for the other two cases.

1000) case, the phase shift from MOI option 1 remains very small. The intensity profiles calculated by MOI option 1 and *HYBRID* almost coincide with each other. On the other hand, the phase shift and intensity profiles calculated using MOI option 2 do not agree with the other two methods at all. When figure errors are large, as in the high-frequency case, ray crossing starts to occur in the local ray tracing. The figure errors not only change the values of the path length but also change the reflecting direction. The indexes of the elements cannot be matched from the incident plane to the exit plane directly, and this condition gives incorrect results for carrying out equation (4). Therefore, one has to use the phase projection MOI method or the direct Fresnel integration (Shi *et al.*, 2014*b*) in this case.

For the rest of the paper, MOI option 2 was used for all calculations. Let us consider a mirror having figure errors in the medium and low frequencies (0.005–0.5 mm^{-1}, $n = 1–100$) [*cf.* Fig. 5(a)] with the same RMS height error of 2.3 nm as in Fig. 4. The intensity profiles at the image plane with and without figure errors are shown in Fig. 5(b). The multiple maxima near the central peak are due to the low spatial frequency figure errors. Fig. 5(c) shows the local degree of coherence between the central focal point (maximum inten-

Table 1

Global degree of coherence (G) extracted from the MOI model using equation (8) and the RMS beam size at different beam locations.

	Without figure error		With figure error	
	G	RMS beam size (µm)	G	RMS beam size (µm)
Source plane	0.16	2	0.16	2
Incident plane (full beam)	0.16	899	0.16	899
Incident plane (mirror accepted)	0.70	152	0.70	152
Exit plane	0.70	178	0.70	177
Image plane (full beam)	0.71	0.035	0.71	0.048
Image plane (within 50 nm range)	0.88	–	0.87	–

sity) and any point at the image plane. The curve without figure errors (solid line) is near symmetric around the beam center, while that with figure errors (dotted line) is not. This finding implies that the coherence property is redistributed by the figure errors. Note that the position where the local coherence is 1 in Fig. 5(c) is the same as the position with maximum intensity in Fig. 5(b). The width of the central peak defines the coherent area of the beam, which is important information for beamline and experimental design. Fig. 5(d) presents the distribution of the cosine of the wavefront phase at the image plane. There is a broad flat peak (plane wave) in the center for the case without figure errors. The one with figure errors has a much narrower flat peak, which is a clear indication that figure errors damage the wavefront and decrease the size of its plane wave zone. The size of the plane wave zone without figure errors is approximately 90 nm, while that with figure errors is only 50 nm.

The global degree of coherence at different beam locations is extracted from the MOI model using equation (8) and the results are summarized in Table 1. The global degree of coherence remains the same from the source plane to the
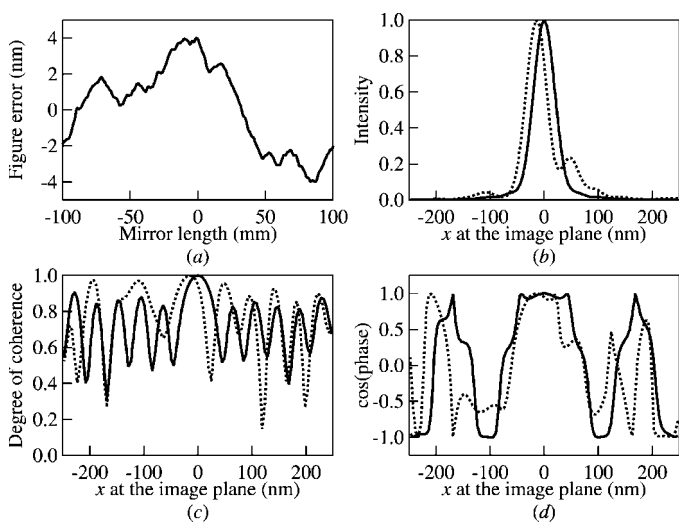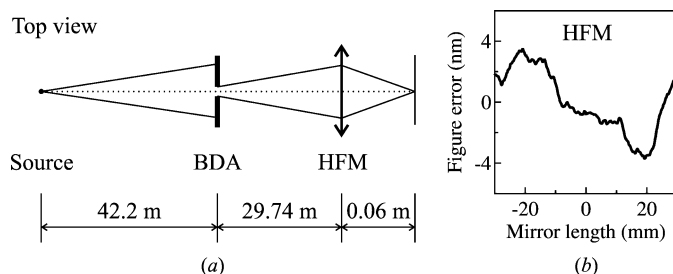

Figure 5

(a) The height error profile of the mirror generated using equation (11) with $b_0 = 1.1 \times 10^{-3}$ nm, $n = 1–100$. (b) Intensity profiles, (c) local degree of coherence and (d) wavefront distribution at the image plane calculated by MOI option 2 through the elliptical cylinder mirror with (dotted lines) and without (solid lines) figure errors. The numbers of elements used in the MOI calculation are the same as listed in the caption of Fig. 2.

mirror incident plane because the free-space propagation does not change the coherence property of the beam. The global degree of coherence at the incident plane within the mirror acceptance is increased to 0.7 since only part of the beam is accepted by the mirror. This value remains the same at the exit plane after wave propagation through the mirror with and without figure errors. Even though figure errors redistribute the local coherence (correlation between different points) and the wavefront of the beam, as shown in Figs. 5(b) and 5(c), they do not change the global beam coherence. At the image plane, the full beam has the same global coherence as at the exit plane disregarding the existence of figure errors. The only way to improve the coherence of the beam is to cut its dimension. As shown in Table 1, the global degree of coherence is 0.88 within the 50 nm range around the central peak, in comparison with 0.71 for the full beam at the image plane.

4. Benchmarking the MOI model against *HYBRID* and *SRW*

We use a previously reported case as an example (Shi *et al.*, 2014a) to benchmark the MOI model. Fig. 6(a) is a replot of a schematic of the beamline layout with the Advanced Photon Source undulator A source, a beam-defining aperture (BDA) and a horizontal focusing mirror (HFM) having an elliptical cylinder shape. By adjusting the size of the BDA, the beam can be turned from fully coherent to partially coherent. The RMS source size and RMS divergence at 10 keV energy are $\sigma_x =$ 274.3 µm and $\sigma_x' =$ 12.4 µrad, respectively. The transverse coherence length at the source is $\xi_x = 1.59$ µm, obtained from equation (10). The global degree of coherence is $G = 0.009$ at the source plane. Due to the low coherence at the source plane, it was separated into a large number (3000) of equal elements in order to satisfy the Fresnel condition. The HFM, which has a length of 60 mm and a grazing angle of 2.5 mrad, images the BDA at the image plane. Fig. 6(b) shows the figure error profile used in the calculation and generated with equation (11). Substituting $n = 1$–600, $s_0 = -3.0$ and $b_0 = 5.6 \times 10^{-3}$ nm into this equation yields an RMS height error of 2 nm.
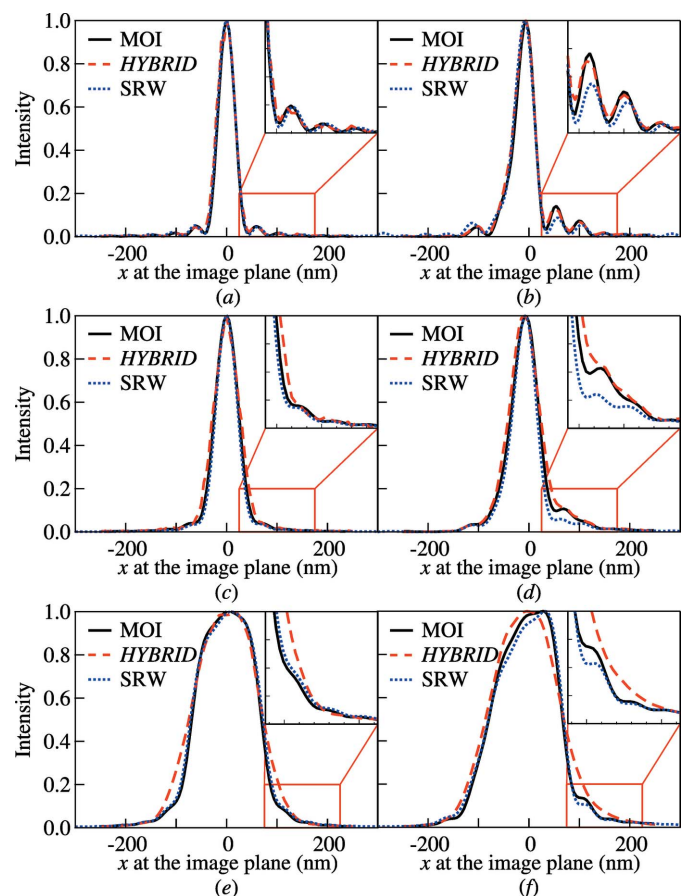
Fig. 7 shows the simulated intensity profiles at the image plane calculated with the MOI model (solid lines), *HYBRID* (dashed lines) and the multi-electron *SRW* (dotted lines) with

BDA sizes of (a, b) 10.5 µm, (c, d) 31.5 µm and (e, f) 84 µm. The figures on the left and right side present results without and with figure errors, respectively. In all of the simulated intensity profiles the MOI model and *SRW* give results in very close agreement, even within the enlarged region around the side lobes. *HYBRID* tends to smooth the side lobes out and overestimate the beam size, which is anticipated owing to the model's intrinsic approximation of the convolution steps. However, the deviation is within most of the beamline design tolerances.

The coherence properties extracted from the MOI model are summarized in Table 2. Through the 42.2 m free-space propagation, the global degree of coherence remains at 0.009. By changing the size of the BDA, with the concomitant flux loss, the beam coherence can be controlled. The global degrees of coherence after the BDA are 0.47, 0.18 and 0.07 for BDA sizes of 10.5 µm, 31.5 µm and 84 µm, respectively. The finite size (60 mm) of the elliptical cylinder mirror further reduces the beam acceptance and increases the beam coher-

Figure 7
Intensity distribution at the image plane calculated using the MOI model (solid lines), *HYBRID* (dashed lines) and the multi-electron *SRW* (dotted lines) with different BDA sizes of (a, b) 10.5 µm, (c, d) 31.5 µm and (e, f) 84 µm. Plots (a), (c) and (e) are calculated by using an ideal elliptical cylinder, while (b), (d) and (f) included the figure error profile shown in Fig. 6(b). The insets show enlarged regions of the intensity profiles. The number of elements used in the MOI calculation are 3000, 300, 300, 300 and 100 at the source, BDA, HFM incident, HFM exit and image planes, respectively.

Figure 6
(a) Schematic of the optical layout and (b) the figure-error profile of the horizontal focusing mirror (HFM). BDA: beam-defining aperture. This is a replot of Fig. 8 of Shi *et al.* (2014a).

Table 2
Global degree of coherence (G) using equation (8) and the RMS beam sizes at different beam locations in Fig. 6(a).

	Without figure error		With figure error	
	G	RMS beam size (µm)	G	RMS beam size (µm)
Source plane	0.009	274.3	0.009	274.3
Before BDA	0.009	584	0.009	584
After 10.5 µm BDA	0.47	–	0.47	–
After 31.5 µm BDA	0.18	–	0.18	–
After 84 µm BDA	0.07	–	0.07	–
Image plane 10.5 µm BDA	0.95	0.034	0.95	0.044
Image plane 31.5 µm BDA	0.59	0.038	0.59	0.047
Image plane 84 µm BDA	0.26	0.056	0.26	0.063

Figure 8
Normalized flux (open circles) and the reciprocal of the global degree of coherence (solid circles) as a function of the BDA size calculated by the MOI model. The lines are provided as a visual aid.

ence. The global degrees of coherence at the image plane are 0.95, 0.59 and 0.26 for the three BDA sizes above, respectively. For the BDA size of 10.5 µm, the beam at the image plane is nearly fully coherent. The diffraction effects from the mirror size and figure errors are apparent, shown as clear side lobes around the central peak in Fig. 7(a).

Fig. 8 shows the relative flux (open markers) and $1/G$ (solid markers) at the image plane as a function of the BDA size. The flux numbers are normalized to the one with the BDA size of 115.5 µm. The flux is nearly linearly proportional to the BDA size, because the BDA size is still much smaller than the near-Gaussian beam size. On the other hand, the global degree of coherence is inversely proportional to the BDA size over the calculated range. The results shown in the figure demonstrate that over a range of apertures one can linearly exchange flux against $1/G$. This inverse linear relation between G and BDA size breaks at the two extremes. When the BDA size is even smaller, the global degree of coherence will reach its upper limit of 1. When the BDA size is greater than 100 µm, the degree of coherence at the image plane reaches a lower limit of 0.2, which is due to the finite acceptance of the 60 mm-long mirror.

The major aim of the MOI model is to provide the full coherence property of the beam at any location. Fig. 9 shows the local degree of coherence and the absolute value of MOI between any two points (x_1 and x_2 on the horizontal axis) at the image plane for the case with a BDA size of 31.5 µm. The band-like structure along the diagonal direction in the local degree of coherence [cf. Figs. 9(a) and 9(b)] defines the area with high degree of coherence, the width of which is the local coherence length. The periodic oscillation of the local coherence comes from the diffraction of BDA and the mirror size. With figure errors [cf. Fig. 9(b)], the local degree
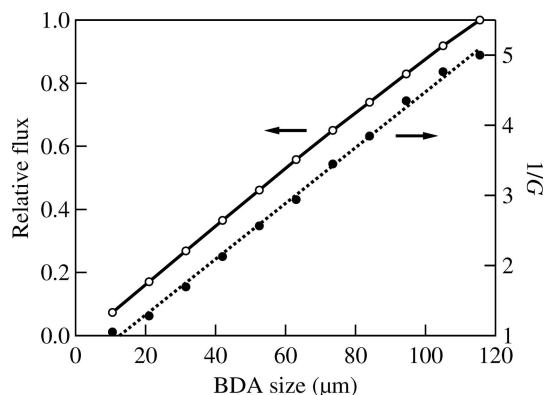
of coherence is redistributed with the high coherence region shifted to the negative x position. Figs. 9(c) and 9(d) are the absolute values of the MOI, which depict the intensity-weighed correlation between every two points. The diagonal lines along $x_1 = x_2$ are the intensity profiles shown in Figs. 7(c) and 7(d), respectively.

We have shown that the MOI model can be very accurate in simulating X-ray beams with all coherence conditions. The efficiency of the program is the other important aspect, especially for the beamline design. We take the above case
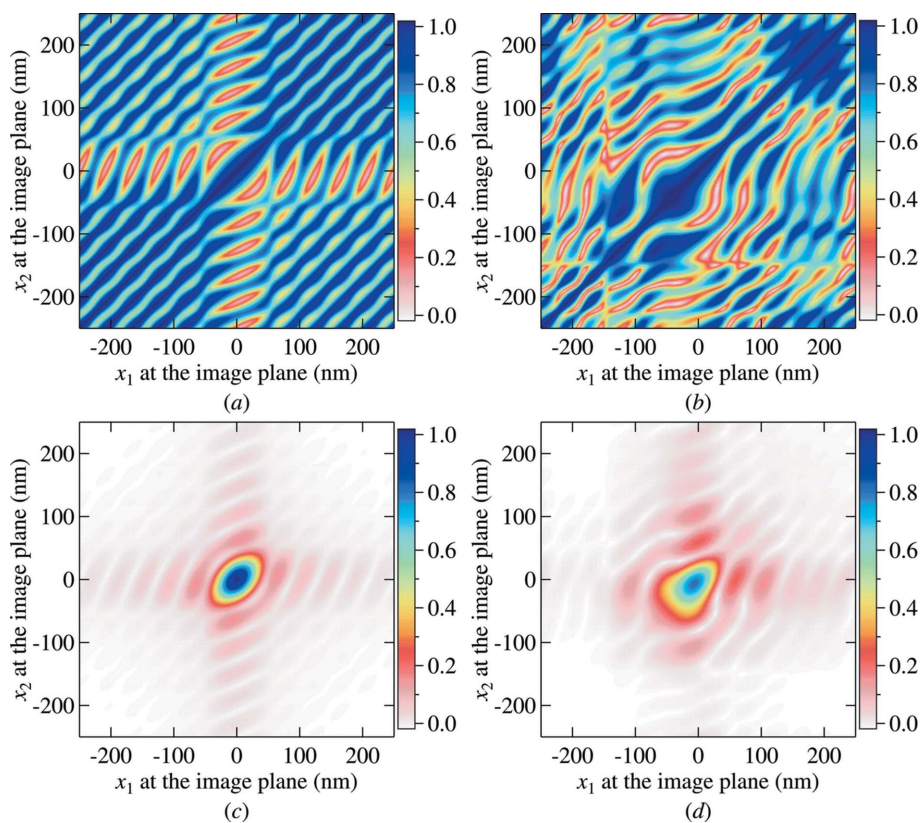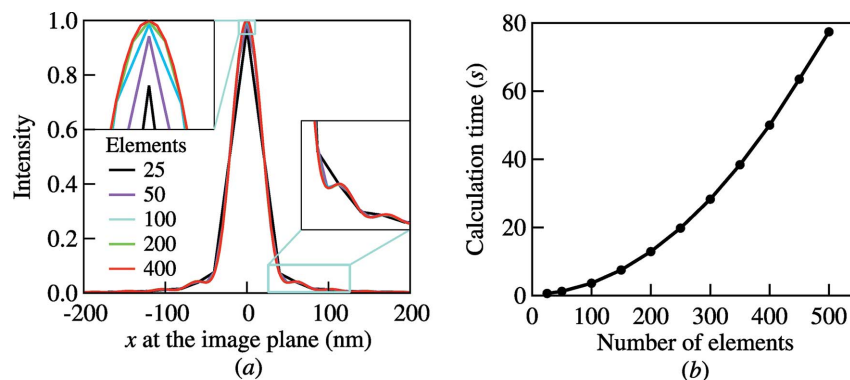

Figure 9
Local degree of coherence between every two points (x_1 and x_2 on the horizontal axis) at the image plane obtained (a) without and (b) with figure errors, respectively. Absolute value of MOI between every two points calculated (c) without and (d) with figure errors, respectively.

Figure 10
(*a*) Intensity profiles calculated by the MOI model with different numbers of elements. The insets show enlarged regions of the intensity profiles. (*b*) Calculation time as a function of the number of elements.

with a BDA size of 21 μm to study the effects of the element size, or the number of elements. For simplicity, the wavefront at the BDA, HFM and image plane are all separated into the same number of elements. Figs. 10(*a*) and 10(*b*) show the simulated intensity profiles and the calculation time, respectively, with different numbers of elements. The MOI simulations were performed on a laptop computer with a single CPU core (i5-2400, 3.1 GHz) and 4 GB RAM. Since the *SRW* calculation was performed in two dimensions and on a workstation, the computation time was not compared directly here. As the number of elements increases, the accuracy of the simulation improves at a cost of calculation time. In this particular case, calculation with 50 elements already gives less than 1% deviation from that with 400 elements. The calculation time with 50 elements is only 1.2 s in comparison with 50 s for the case with 400 elements. Therefore, one can choose between the accuracy and efficiency of the MOI model by varying the number of elements at each calculation plane. This merit makes the MOI model a powerful tool for the beamline design and optimization. In general, the number of elements needs to be sufficient to make sure that the element size is smaller than the coherence length at the calculation plane. For a mirror surface profile with figure errors, the element size also needs to be smaller than the smallest spatial error period. All the above MOI calculations were in one dimension to show the validity of the MOI model. For the one-dimensional and two-dimensional simulations, the calculation time is generally proportional to the second and fourth power of the number of elements in one axis, respectively. More optimizations can be made in the two-dimensional simulation to reduce the calculation time.

5. Conclusions

The MOI model is a full coherence simulation method utilized to propagate the partially coherent radiation through X-ray optics. In this paper, the MOI model is extended to include reflecting mirrors with figure errors. The two methods dealing with figure errors, namely the phase projection and direct path length methods, are both based on local ray tracing. The phase projection method, which is the same as that used in *HYBRID*, represents figure errors as phase shifts added to the amplitude transmission function, while the direct path length method directly calculates the path length from ray tracing through the mirror with figure errors. As long as there is no ray crossing in the local ray tracing process, both methods give the same results.

The major advantage of the MOI model is its ability to provide coherence information along the beamline as well as intensity profiles. By comparing the MOI propagation with and without figure errors, we confirm that low-frequency figure errors contribute to the multiple maxima near the central peak, redistribute the local coherence of the beam, and distort the wavefront. However, figure errors do not change the global degree of coherence unless the beam is cut.

The MOI model is benchmarked against *SRW* and *HYBRID*. The MOI model can provide accurate results in different coherence conditions. Since the full MOI is stored at any calculation plane, sequential simulation of beamline optics can be realised, which is difficult for the multi-electron *SRW*. Furthermore, the accuracy and efficiency of the MOI model can be balanced by simply changing the number of elements within the wavefront. These merits make the MOI model an ideal tool for advanced beamline simulation, especially for beamlines that rely on the coherence properties of the beam.

References

Bahrdt, J. (2007). *Phys. Rev. ST Accel. Beams*, **10**, 060701.
Born, M. & Wolf, E. (1999). *Principles of Optics*. Cambridge University Press.
Canestrari, N., Chubar, O. & Reininger, R. (2014). *J. Synchrotron Rad.* **21**, 1110–1121.
Chubar, O. (2014). *Proc. SPIE*, **9209**, 920907.
Goodman, J. (2015). *Statistical Optics*. New York: John Wiley and Sons.
Hua, W.-Q., Bian, F.-G., Song, L., Li, X.-H. & Wang, J. (2013). *Chin. Phys. C.* **37**, 068001.
Mandel, L. & Wolf, E. (1995). *Optical Coherence and Quantum Optics*. Cambridge University Press.
Marr, G. (2013). *Handbook on Synchrotron Radiation: Vacuum Ultraviolet and Soft X-ray Processes*. Elsevier.
Meng, X., Xue, C., Yu, H., Wang, Y., Wu, Y. & Tai, R. (2015). *Opt. Express*, **23**, 29675–29686.
Nugent, K. A. (2010). *Adv. Phys.* **59**, 1–99.

Pelliccia, D., Nikulin, A. Y., Moser, H. O. & Nugent, K. A. (2011). *Opt. Express*, **19**, 8073–8078.

Samoylova, L., Buzmakov, A., Geloni, G., Chubar, O. & Sinn, H. (2011). *Proc. SPIE*, **8141**, 81410A.

Sanchez del Rio, M., Canestrari, N., Jiang, F. & Cerrina, F. (2011). *J. Synchrotron Rad.* **18**, 708–716.

Shi, X., Assoufid, L. & Reininger, R. (2016). *Proc. SPIE*, **9687**, 968703.

Shi, X., Reininger, R., Sanchez del Rio, M. & Assoufid, L. (2014a). *J. Synchrotron Rad.* **21**, 669–678.

Shi, X., Reininger, R., Sánchez del Río, M., Qian, J. & Assoufid, L. (2014b). *Proc. SPIE*, **9209**, 920909.

Siewert, F., Buchheim, J., Boutet, S., Williams, G. J., Montanez, P. A., Krzywinski, J. & Signorato, R. (2012). *Opt. Express*, **20**, 4525–4536.

Singer, A. & Vartanyants, I. A. (2014). *J. Synchrotron Rad.* **21**, 5–15.

Stephenson, G. B., Robert, A. & Grübel, G. (2009). *Nat. Mater.* **8**, 702–703.

Vartanyants, I. A. & Singer, A. (2010). *New J. Phys.* **12**, 035004.

Vartanyants, I. A. & Singer, A. (2016). *Synchrotron Light Sources and Free-Electron Lasers*, edited by E. J. Jaeschke, S. Khan, J. R. Schneider and J. B. Hastings, pp. 821–863. Springer International Publishing.

Zhang, P., Yang, S., Wang, L., Zhao, J., Zhu, Z., Liu, B., Zhong, J. & Sun, X. (2014). *Nanotechnology*, **25**, 245301.